Kim *et al. AAPPS Bulletin* (2022) 32:15
https://doi.org/10.1007/s43673-022-00045-4

AAPPS Bulletin

REVIEW ARTICLE Open Access

Review of technical achievements in PAL-XFEL

Changbum Kim[1*], Sung-Ju Park[1], Chang-Ki Min[1], Jinyul Hu[1], Sang-Hee Kim[1], Youngdo Joo[1], Hoon Heo[1], Dong-Eon Kim[1], Sojeong Lee[1], Heung-Sik Kang[1], In Soo Ko[1], Moonsik Chae[2] and Jaehyun Lee[2]

Abstract

The X-ray Free Electron Laser of Pohang Accelerator Laboratory (PAL-XFEL) was opened for the user in 2017. PAL-XFEL was the third XFEL facility in the world and well known for the small timing jitter of FEL radiation. This success was possible because of the significant achievements in the accelerator technology in PAL-XFEL. They are not limited to a small part of the accelerator but cover from the injector for the electron beam generation to the undulator line for FEL radiation. In this review, we describe the details of newly developed devices that contributed to the successful construction of PAL-XFEL.

Keywords: Hard X-ray, Free Electron Laser, PAL-XFEL, PAL

1 Introduction

During the last two decades, the hard X-ray Free Electron Laser (XFEL) has made big progress in the accelerator community. In 2009, Linac Coherent Light Source (LCLS) at SLAC national accelerator laboratory was constructed for the first time in the world [1]. The big success of the XFEL strongly motivated the world to build new facilities. After 2 years, SPring-8 Angstrom Compact free electron LAser (SACLA) was constructed in Japan [2, 3]. The XFEL of Pohang Accelerator Laboratory (PAL-XFEL) started the user service in 2017 [4, 5] and European XFEL was opened for the public in the same year at Deutsches Elektronen Synchrotron (DESY) using the superconducting technology [6]. Swiss FEL of Paul Scherrer Institut (PSI) started regular user service in 2019 [7]. In addition to that, LCLS-II and Shanghai HIgh repetition rate XFEL aNd Extreme light facility (SHINE) are under construction to obtain MHz repetition rates from the superconducting technology [8, 9].

The series of XFEL constructions show that the XFEL requires strong government support and advanced accelerator technologies in a large accelerator laboratory based on a long historical background. In this sense, PAL-XFEL is remarkable in many aspects. Before the PAL-XFEL construction, a 3 GeV synchrotron radiation facility, Pohang Light Souce (PLS), was running in Korea and just finished the upgrade program (PLS-II) in 2011 [10–12]. At the same time, the PAL-XFEL construction was started in 2011 and finished in 2016 with a 400 million USD budget. Just after starting the user service in 2017, PAL-XFEL became famous for its excellent FEL stability and small arrival timing jitter [5]. Table 1 shows the specification of PAL-XFEL parameters. This means that a significant amount of effort was devoted to the construction of a successful machine, and many technical achievements were made during the short construction time of PAL-XFEL.

In this paper, we review improvements in the accelerator technology of PAL-XFEL. It covers new developments from the photocathode radio-frequency (RF) gun for the electron beam generation to the undulator line for the FEL radiation. These improvements made on-time, on-budget construction possible and have become a foundation of the stable operation of PAL-XFEL.

2 Injector

2.1 Injector physics

The PAL-XFEL injector consists of a photocathode RF gun, a laser system, two accelerating structures with two

*Correspondence: chbkim@postech.ac.kr
[1]Pohang Accelerator Laboratory, POSTECH, Pohang 37673, Korea
Full list of author information is available at the end of the article

Table 1 Specifications of PAL-XFEL

Parameters	Specifications
Beam energy	10 GeV
Energy spread	$\sim 10^{-4}$
Beam charge	200 pC
Peak current	3 kA
Bunch length	10 ∼ 60 fs
Repetition rate	60 Hz
Hard X-ray wavelength	0.06 ∼ 1 nm
Soft X-ray qavelength	1 ∼ 10 nm
Photon flux @ 0.1 nm	0.44×10^{12} photons/pulse

sets of klystron-modulator systems, magnets, and various diagnostic instrumentations. The PAL-XFEL injector is required to provide electron beams with the projected emittance of 0.5 mm mrad, bunch charge of 200 pC, beam energy of 135 MeV, and repetition rate of 60 Hz as summarized in Table 2 [13, 14]. Since the beam emittance together with the slice energy spread and peak current have a significant influence on the FEL gain length and saturation power [15], an injector test facility (ITF) for PAL-XFEL was constructed to confirm the beam performance. In addition to the electron beam generation from the photocathode RF gun, emittance minimization of the injector lattice, energy spread control using a laser heater, bunch length measurement with a deflecting cavity, and other diagnostic systems such as beam position monitors, beam profile monitors, and beam charge monitors were evaluated in ITF.

ITF was established in a new building built by expanding an existing test lab for the PLS-II facility. The accelerator tunnel is made of 0.8 ∼1.5 m thickness concrete walls and ceilings. The size of the tunnel's inner space is 19.2 m long, 3.5 m wide, and 2.4 m high. The laser room is located close to the gun to minimize the optical transport line, and a 0.8 m thickness concrete wall divides the laser room and the accelerator tunnel. A control room is prepared on the second floor of the laser room. Various monitoring and control signals are provided by Experimental-Physics-and-Industrial-Control-System (EPICS). Cooling water with temperature stability of ± 0.1°C is supplied by an independent cooling station outside the ITF building. Figure 1 shows accelerator structures inside the ITF tunnel [16].

Table 2 Specifications for the PAL-XFEL Injector

Parameters	Specifications
Energy	135 MeV
Charge	200 pC
Emittance	< 0.5 mm mrad
Bunch Length	∼ 3 ps
Repetition Rate	60 Hz

The emittance of the generated electron beam is determined by the RF phase at the gun cathode, gun cavity shape, and drive-laser parameters. Just after the electron gun, the beam passes through the space charge dominant regime before entering the first acceleration section, and the gun solenoid controls the beam against the space charge effect. In addition, the beam emittance can be affected by the first accelerating column position and their field strengths.

The position and the strength of the solenoid magnet were determined by the emittance compensation process [17]. In the PAL-XFEL injector, a 0.2-m long solenoid is positioned after the photocathode RF gun, of which the field center is at 0.206 m from the cathode surface, and the nominal on-axis field is 0.25 T at the longitudinal field center. The first accelerating column starts at 2.2 m from the cathode and the position was chosen by the simulation result of the layout optimization. The columns are set to the on-crest phase for maximum energy gain. The beam reaches 70 MeV after the first accelerating column and 135 MeV after the second column. By increasing the beam energy through the accelerating columns, the space charge force becomes weaker, and the beam emittance is kept small at the injector end [18].

2.2 Photocathode RF gun

Photocathode RF guns are widely used as the electron beam source in the XFEL facilities [19–22]. In PAL-XFEL, a 1.5 cell S-band photocathode-RF-gun made of oxygen-free-high-conductivity (OFHC) copper generates a 120 MV/m electric field gradient at the gun cathode to make the electron beam of 5 MeV energy [23]. In the photocathode RF gun, however, time-dependent transverse deflection of each electron due to the Lorentz force in the cavity can increase the transverse emittance [24]. The third-generation Brookhaven-National-Laboratory (BNL) gun is designed to feed RF power into

Fig. 1 Inside of the ITF tunnel. Two accelerating columns and solenoid magnets are shown

the gun using a single coupling hole [25, 26], and the one-sided coupling scheme causes asymmetry in the electromagnetic field inside the cavity. The asymmetric field can be expanded into multi-pole fields, and the dipole and quadrupole fields are the main sources of the emittance growth [27, 28].

Minimization of the multi-pole RF field has been investigated in the design of the state-of-the-art photocathode RF gun, which aims to produce high-brightness electron beams [25, 27]. For example, a racetrack-shaped gun cavity was introduced to reduce the multi-pole mode in the photocathode RF gun of LCLS [29, 30]. In PAL-XFEL, a photocathode RF gun with four holes was proposed to reduce the multi-pole mode [31–34]. The second cell of the gun cavity has a dual side coupler and two pumping ports for better RF field symmetry, and they play the same role as the racetrack-shaped cavity in the LCLS gun [35]. Figure 2 shows the photocathode RF gun of PAL-XFEL.

In the PAL-XFEL injector, a Ti:Sapphire laser was installed as a drive laser for the photocathode RF gun. The laser can produce a 10-mJ infrared (IR) laser pulse at 760-nm wavelength and the IR laser pulse passes through a third harmonic generator to produce a 256-nm ultraviolet (UV) pulse for the electron beam generation. The spatial and temporal shapes of the laser pulse were optimized experimentally in the ITF facility. A laser pulse with a 0.175-mm beam size was used to generate a 200 pC bunch charge and the measured emittance was 0.33 mm mrad in both the horizontal and vertical directions. When the beam size was increased to 0.218 mm, measured emittances were 0.45 and 0.50 mm mrad in the horizontal and vertical directions, respectively. The measurement result showed that a smaller laser beam size at the gun cathode generates a lower projected emittance at the injector end. In addition, different laser pulse widths were tried to generate electron beams and a minimum emittance was obtained with a 3-ps pulse width. On the other hand, in the simulation result for the transverse laser profile, the truncated Gaussian profile showed a remarkably lower slice emittance compared to the uniform round one case. The measured emittance in ITF was smaller than the simulation result of the uniform transverse profile and bigger than that of the 1σ truncated Gaussian. More precisely, the measured emittance was between the simulation results of the 0.6σ and 0.7σ truncated Gaussian profiles [36].

2.3 Laser heater

After the electron beam is accelerated to beam energy above several hundred MeV where the electron beam becomes less sensitive to the space charge effect, the electron beam is compressed by magnetic bunch compressors. The bunch length becomes shorter by a factor of 100 through the compression in the XFELs, but the beam quality can be impaired by the collective effects at the same time. Coherent synchrotron radiation (CSR) with a wavelength shorter than the bunch length amplifies the density modulation leading to longitudinal microbunching instability (MBI). CSR-induced MBI was studied analytically [37, 38] and numerically [39, 40]. The microbunching gain is sensitive to the uncorrelated energy spread, and a laser heater was proposed to suppress the instability by controlling the uncorrelated energy spread before entering the first bunch compressor [41, 42]. Laser heaters have been used at LCLS [43], FERMI at Elettra [44], European-XFEL [45], and SwissFEL [46].

The laser heater consists of a 0.5-m long undulator and a magnetic chicane with four dipoles as shown in Fig. 3. The undulator has planar permanent magnets with a 50-mm period and a 25-mm minimum gap. The undulator gap is changed by moving the upper and lower magnets simultaneously, and the gap can be controlled remotely with a 5 μm accuracy. Less than 10% of the IR laser power from the driver laser of the photocathode RF gun is used for the laser heater. The laser pulse energy can be adjusted by an attenuation polarizer and the maximum energy is 223 μJ.

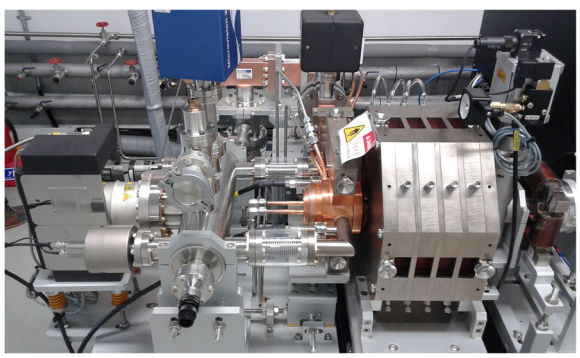

Fig. 2 The photocathode RF gun of PAL-XFEL

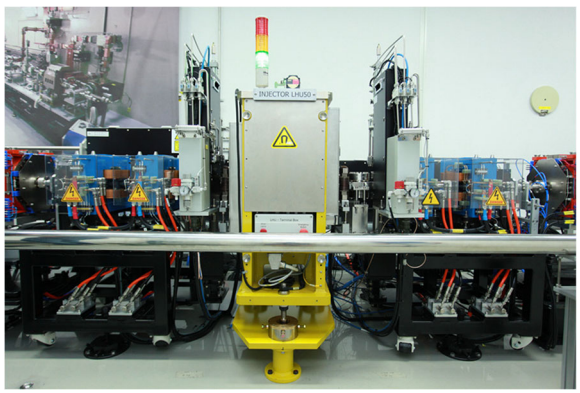

Fig. 3 The laser heater of PAL-XFEL. Four dipole magnets are shown before and after the undulator (yellow color)

Parameters of the PAL-XFEL laser heater are summarized in Table 3.

Spatial overlap between the laser pulse and electron bunch was achieved by controlling the electron and laser at the screens both upstream and downstream of the undulator. Two sets of correctors for the horizontal and vertical beam steering are installed both upstream and downstream of the undulator. The electron beam size in the undulator can be adjusted using the four quadrupoles upstream of the laser heater. The measured electron beam sizes were 197 μm and 192 μm at the entrance and exit of the undulator, respectively. For the laser alignment, two motorized mirrors installed on the linear stages are controlled remotely to change the laser beam path. The incident laser beam size is remote-controlled by a motorized focusing lens. The laser beam size was about 211 μm in the middle of the undulator.

The laser pulse and the electron bunch were temporally overlapped by controlling the laser delay stage. First, a photodiode is installed after the IR laser exit viewport, and a rough overlap was made using the photodiode signal up to the photodiode response time (a few tens of ps). Next, the uncorrelated energy spread of the electron beam was used for fine-tuning. The S-band deflector downstream of the first bunch compressor streaks the electron bunch to the vertical direction and the following spectrometer dipole bends the bunch by 30° to the horizontal direction. The temporal overlap was obtained at the delay for the maximum energy spread [47].

3 Linear accelerator

3.1 RF timing system

The low-phase-noise performance of the RF timing system is linked directly to the resolution and accuracy of the RF phase measurement and feedback in the low-level RF (LLRF). In addition, synchronizing between the injector laser and the reference S-band signal plays a critical role in the FEL jitter performance because the change of the laser arrival time is equivalent to the phase changes of all RF stations, which makes jitter in both the electron beam energy and energy chirp.

Table 3 Specifications of the PAL-XFEL laser heater

Parameters	Specifications
Laser wavelength	760 nm
Laser beam size	221 μm
Laser pulse width (FWHM)	8 ps
Laser pulse energy	< 250 μJ
Electron beam energy	135 MeV
Electron beam size	192 μm
Electron bunch length	3.6 ps
Dipole bending angle	5.82 deg
Undulator period	50 mm
Number of undulator period	9
Undulator minimum gap	25 mm
Undulator parameter at 28.66 mm gap	1.5

The RF timing distribution is based on a 476-MHz reference signal, which is locked to a 10-MHz rubidium and oven-controlled crystal oscillator (OCXO) to improve the frequency stability and reduce the phase noise in the offset frequency from 1 Hz to 10 MHz. The 476 MHz reference signal is distributed to 16 locations in the linac over a 1.5-km distance including the soft X-ray branch. A low loss, vibration resistant, hard corrugated copper cable is used for RF signal distribution and a water-cooled duct is installed to minimize the thermal expansion of this cable. The stability of the cooling water temperature is 29±0.1°C and the temperature inside the duct is maintained within 0.1°C. The measured data showed that the rise of the temperature of 0.05°C gave the additional phase delay of 0.2°, and the measured timing drift of the linac was less than 1 ps peak-to-peak stability for one week.

At each location, a 476-MHz signal is converted to a 2.856-GHz signal using a phase-locked dielectric resonator oscillator (PLDRO), which is developed by RUPPtronik, and a 2.856-GHz signal is amplified to drive LLRFs and additional diagnostic systems such as beam arrival-time monitors. The integrated phase noise of the S-band was measured as small as 1 fs from 1 kHz to 10 MHz offset. The differential phase noise was also estimated to be 1 fs from 1 Hz to 1 MHz offset. The rack temperature for the PLDRO is stabilized to 26 ± 0.1°C.

The phase noise was measured between the Ti:Sapphire laser and a free-running 2.856 GHz PLDRO. A balanced phase detector was built using a Sagnac interferometer to measure the phase difference between optical pulses and S-band RF [48]. The optical group delay inside the interferometer can be modulated by RF to measure the phase difference with high sensitivity. The integrated relative phase jitter from 1 Hz to 100 kHz offset frequency was estimated to be less than 20 fs [49].

3.2 RF power source

A start-to-end simulation using Elegant code [50] was carried out to find the stability requirements of the amplitude and phase of the linac RF system. The simulation result showed that less than 10% bunch current jitter $|\Delta I/I_0|$, less than 0.02% energy jitter $|\Delta E/E_0|$, less than 20 fs arrival-time jitter $|\Delta t|$, and less than 5% emittance jitter $|\varepsilon/\varepsilon_{n0}|$ are required to achieve a highly stable electron beam at the entrance of the undulators [51]. The most stringent requirements for the S-band RF system are less than 0.02% amplitude jitter and less than 0.03° phase jitter. In addition, the amplitude and phase stabilities for the X-band linearizer are 0.06% and 0.1°, respectively. To meet

the requirement, the pulse-to-pulse RF stability, determined by the klystron beam voltage, should be as stable as 50 ppm to achieve the phase stability of 0.03° and 0.1° for the S-band and X-band RF, respectively.

To improve the stability of the charged voltage in the pulse-forming network (PFN) capacitor of the modulator, an inverter power supply was used with an insulated-gate bipolar transistor (IGBT) switch (switching speed of 30 $\sim$ 50 kHz). Overshooting of the charged voltage was minimized as much as possible using four parallel inverter-power-supplies. After the PFN voltage reached its target value, switching of the inverter power supply is stopped for 200 $\sim$ 500 μs, and a thyratron switch is turned on to generate a high-voltage pulse for a klystron. In this way, the PFN voltage during the idling time is kept as stable as 10 ppm rms, and the voltage stability of the modulator, which determines RF stability, was measured to be 30 ppm rms. 200 MW (400 kV, 500 A) modulator output is provided to a commercial klystron (E37320) to generate 80 MW S-band RF-power. The RF frequency is 2856 MHz and the pulse width is 4 μs. To prevent the damage from the high power RF, the klystron has two output windows at two RF ports, and RF power is recombined using a magic tee waveguide. The measured amplitude and phase stabilities of the S-band RF were 0.02% and 0.03° rms, respectively. The measurement result of the electron-beam energy jitter was 0.02% rms at the linac end when two bunch compressors were used [52]. The specifications of the modulator are summarized in Table 4, and Fig. 4 shows the modulator and klystron for PAL-XFEL.

The newly developed LLRF system for PAL-XFEL consists of three parts: RF front-end modules, analog-digital-converter field-programmable gate array (ADC-FPGA) boards, and an industrial personal computer (PC). RF front-end modules generate local and clock RF signals, modulate RF pulses to feed the SSA, and demodulate RF signals received from various points of the RF station. ADC-FPGA boards convert analog signals from RF front-ends and several other devices into digital signals. This board processes digital signals and communicates with the industrial PC. The industrial PC has an i7 Central-Processing-Unit (CPU) and a touchscreen panel, which has cost-effectiveness and high performance. The industrial PC has a real-time Linux operating system to process all the data in real-time and runs an EPICS Input-Output-Controller (IOC) with a local Control-System-Studio (CSS) client. The local display is used for the status monitoring, diagnosis, and data analysis [53].

Table 4 Major specifications of the PAL-XFEL modulator

Parameters	Specifications
Peak power	200 MW
Average charging power	120 kW
Pulse peak output voltage	400 kV
Pulse peak output current	500 A
PFN voltage stability	$<$ 10 ppm
Pulse width	7.5 μs
Plat-top width	4.0 μs
Repetition rate	60 Hz

Fig. 4 The modulator and klystron for PAL-XFEL

3.3 Energy doubler

The electron bunch from the S-band photocathode RF gun is accelerated to high energy using accelerating sections. Each accelerating section has 3-m-long constant-gradient-traveling-wave accelerating columns which are connected to the S-band RF station. Before the first bunch compressor, two accelerating columns are fed by an S-band RF station consisting of a 200-MW modulator and an 80-MW klystron. However, after the first bunch compressor, four accelerating columns are fed by an S-band high-power RF station using an S-band Stanford-Linac-Energy-Doubler (SLED). After the SLED, the klystron output pulse is equally divided into four accelerating columns using three 3-dB power hybrids and terminated with high-power loads to reduce the reflected power to the klystron [54].

The S-band SLED consists of a 3-dB power hybrid and two identical over-coupled cavities resonant at 2856 MHz as shown in Fig. 5. A fast-acting-triggered Phase-Shift-Keying (PSK) π-phase-shifter, which reverses the RF phase of the klystron output power, is inserted into the klystron driveline. In the RF pulse compression process, the cavities store klystron output power during a large fraction of the pulse length. After that, the phase of the klystron output is reversed, and the cavities emit the stored power rapidly into the accelerating section, adding to the given klystron output power during the remaining pulse length. This means that the peak power is enhanced at the expense of the pulse length without increasing the average input power [55–57].

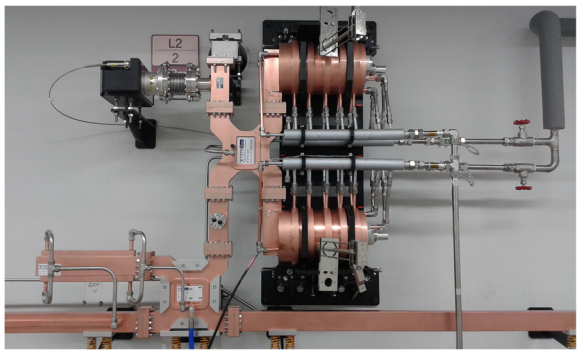

Fig. 5 The SLED for PAL-XFEL. The 3-dB power hybrid and two resonant cavities are shown

The original SLED was first developed in the 1970s when the klystron output power was only around 30 MW, and there had been no significant problem during the PLS operation for more than 15 years. However, the output power of the PLS-II klystron was increased to 60 MW, and high radiation-dose rates were noticed frequently from original SLEDs due to the RF breakdown. In the original SLED, the 3-dB power hybrid is combined with the two cylindrical cavities through the single-iris coupling structure. High radiation-dose rates were measured around the center of the 3-dB power hybrid and the cavity-waveguide coupling iris of the two cavities. Moreover, the S-band RF station of PAL-XFEL requires the RF output peak power of 80 MW with a repetition rate of 60 Hz.

A three-dimensional Finite-Difference-Time-Domain (FDTD) simulation was carried out to estimate the distribution of the electric field and the surface current of the original 3-dB power-hybrid by using CST Microwave Studio (MWS) [58]. The input power was normalized to 1 W, and the calculated magnitude of the electric field had a maximum value of 1470 V/m around the center rods. After the modification of the 3-dB power hybrid of the original SLED, the calculated maximum peak electric field was 700 V/m, which was about one-half of the original structure. The RF performances were checked using a vector network analyzer after the fabrication of forty-two 3-dB power hybrids. The measured mean coupling factor at the first output port of all 3-dB power hybrids was −3.032 dB with a standard deviation of 0.013 dB. The measured mean coupling factor at the second output port was −3.025 dB with a standard deviation of 0.016 dB. The difference between the coupling factors of two output ports of all the fabricated power hybrids was within ±0.04 dB.

To reduce the electron field gradient which causes RF breakdown at the cavity-waveguide coupling iris, a dual-irises side-wall coupling was applied for the new SLED [59, 60]. The dimensions of the new SLED cavity with the dual-irises side-wall coupling were selected to maintain the same coupling coefficient and resonance frequency of the original SLED cavity. The maximum electric field strength of the dual-irises side-wall coupling was calculated to be two-thirds of the single-iris coupling case. This result agreed with the previous measurement result that the electric field amplitude was reduced by 20 ∼ 30% when the dual-irises side-wall coupling was adopted [60].

Since the SLED cavity operates with a higher harmonic mode, the electromagnetic field modes of the cavity should be analyzed to check the mode competition. Table 5 shows the CST-MWS simulation result of various modes around 2856 MHz for a simple cylindrical cavity, with and without groove structure. The cavity radius and the length are 102.55 mm and 335.9 mm, respectively. Note that the TM115 and TE015 modes have degenerated, but the degeneracy can be removed by introducing a groove structure on the endplate of the cavity. The width and depth of the groove are 10 mm and 9 mm, respectively. Moreover, the two coupling irises are separated by 76.5 mm which is one-half of the guide wavelength. This means the phase of the electric field at the two coupling irises is reversed, and the spurious mode like TM115 is difficult to excite. There are two neighboring modes TM023 and TE123 near the TE015 mode, but the Q-value of the TE015 mode is much higher than that. In the case of TE413 and TE016 modes, the mode separations from TE015 are larger than 43 MHz which is large enough to avoid mode competition.

The beam energy gain of each S-band RF station was measured after the third bunch compressor. During this measurement, the klystron peak power of each S-band high-power RF station was set to 65 MW, and the mean energy gain of each RF station was 271 MeV. The same measurement was tried without the SLEDs, and the beam energy gain was 161 MeV. The calculated SLED energy gain was 271/161 ≃ 1.68 which showed good agreement with the expected SLED energy gain of 1.6 for PAL-XFEL [61].

3.4 S-band accelerating structure

The accelerating structure for PAL-XFEL is designed as a constant-gradient traveling-wave accelerator, which

Table 5 Simulation result of resonant mode frequencies around 2856 MHz for the SLED cavity

Modes	No groove (MHz)	With groove (MHz)
TE413	2813.084	2807.533
TE123	2818.769	2818.627
TM115	2856.017	2839.573
TE015	2856.017	2855.962
TM023	2896.305	2860.963
TM016	2901.898	2899.196

is more efficient in the acceleration than the constant-impedance type [62]. For a high group velocity of the traveling wave, the operating mode of $2\pi/3$ was selected as a typical traveling-wave accelerating structure. In this case, disk-loaded circular waveguides, with gradually decreasing irises and cylinders, are used to control the attenuation changes per cell. Table 6 shows the major specifications of the accelerating structure for PAL-XFEL.

A traditional single-feed coupler of the accelerating structure causes a field asymmetry in the coupler cavity, which degrades the electron beam quality due to its multi-pole field components [63]. Since the single RF coupling hole is the main reason for the field asymmetry in the single-feed coupler, symmetric dual coupling holes are preferred to reduce the multi-pole components. However, dual-feed couplers are bigger and more expensive than single-feed couplers owing to the power combiners. As a remedy for these problems, J-type couplers and quasi-symmetric single-feed couplers have been developed by Mitsubishi to deliver two-thirds of the PAL-XFEL accelerating structures [64, 65]. The J-type coupler offers better field symmetry than the quasi-symmetric single-feed coupler. However, the J-type coupler is more difficult to fabricate because of the waveguide structure surrounding the coupler cavity wall, which may cause errors in the tuning of the entire accelerating column. Thus, the J-type coupler was used in the PAL-XFEL injector only, and the quasi-symmetric single-feed coupler was used after the injector. The quasi-symmetric single-feed coupler has a dummy cavity connected through an additional slot that is identical to the power coupling slot and provides a field pattern inside the coupler similar to that of dual-feed couplers. This coupler type is more simple and more compact than J-type couplers or dual-feed couplers to reduce the manufacturing cost.

The rest of the S-band accelerating structures were produced in the collaboration with Vitrotech. In this case, racetrack-shaped, quasi-symmetric single-feed couplers were used to reduce the field asymmetry inside the coupler cavity. The racetrack-shaped coupler was suggested to reduce the quadrupole field components in the coupler cavity [66], and dual-feed racetrack-shaped couplers were used for S-band structures of the LCLS injector. This type of coupler reduced the quadrupole fields more effectively than the dual-feed cylindrical coupler [63]. In PAL-XFEL, the offset between the racetrack centers was optimized to reduce the dipole component in the direction of the input waveguide port. The selected offset values were 70 μm and 20 μm for the input coupler and output coupler, respectively [67]. Figure 6 shows S-band accelerating structures in the PAL-XFEL linac tunnel.

3.5 S-band deflecting cavity

In PAL-XFEL, low-emittance electron beams are compressed to 20 fs using bunch compressors, and transverse deflecting cavities are used to measure the longitudinal bunch length of the electron beam. The first deflecting cavity of PAL-XFEL was produced by RadiaBeam Technologies and installed after the first bunch compressor, but the second and the third deflecting cavities were developed in the collaboration with Vitzrotech. The second deflecting cavity was installed downstream of the third bunch compressor in the hard X-ray linac, and the third deflecting cavity was installed downstream of the bunch compressor in the soft X-ray branch.

The operating frequency and temperature of the deflecting cavity are 2856 MHz and 30°C, respectively. Considering the electron bunch length of 20 fs after the third bunch compressor, the length of the deflecting cavity was designed to be 2.7 m to generate 20 MV deflecting voltage. The HEM011 disk-loaded circular-waveguide-mode is widely used for the deflecting cavity, and a disk structure with two side holes was adapted to suppress the degenerate vertical and horizontal modes as in the LOLA-type deflecting cavity [68, 69]. In this structure, the field mode can be changed from the TM011 mode to the HEM11

Table 6 Major specifications of the PAL-XFEL accelerating structure

Parameters	Specifications
Accelerator type	Constant gradient
Accelerating gradient	$>$ 27 MV/m
Operation frequency	2856 MHz
Operation temperature	30°C
Operation mode	$2\pi/3$
Shunt impedance	$\geq$ 53 $M\Omega$/m
Q	$>$ 13000
Phase error	$< \pm 2.5°$
Overall length	3.120 m

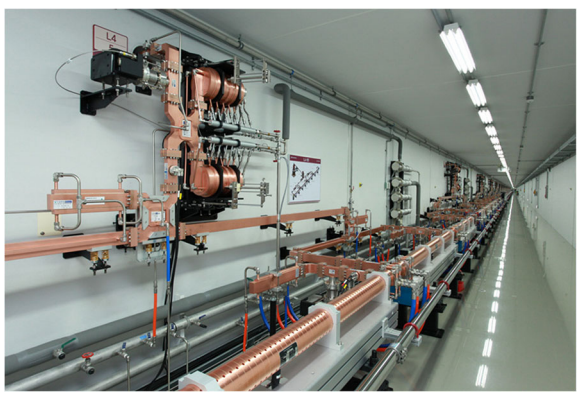

Fig. 6 S-band accelerating structures inside the PAL-XFEL linac tunnel

mode as the ratio of the iris radius to the cavity radius is increased. In consideration of the geometric tolerance and the deflecting field efficiency, 72 identical deflecting cells which work on the $2\pi/3$ traveling wave mode were used to meet the required deflecting voltage of 20 MV and the phase shift per cell. To design the input and output couplers, the internal reflection and the phase advance were calculated using Kroll's method with the 3D electromagnetic field solver of CST MWS [70]. The coupler's cell radius and coupling slot width were optimized to make the internal reflection ratio smaller than 0.02, and the phase difference between the disk's iris was decided to 120° [71]. Table 7 shows the major RF parameters of the deflecting cavity.

3.6 X-band solid state amplifier

The photo-cathode electron gun of PAL-XFEL generates the electron beam with 3 ps bunch length and 5 MeV beam energy. The electron beam is accelerated by the S-band RF normal-conducting accelerating structures up to 135 MeV before the first bunch compressor, which reduces the bunch length about five times. Since the chicane-type bunch compressors use the path-length difference in dispersive bending magnets, the electron beam should be accelerated on the off-crest RF phase to make the energy chirp in the electron beam. In this process, the energy chip of the electron beam becomes nonlinear owing to the amplitude of the sine wave. This nonlinear energy chirp causes non-uniform current profiles after the bunch compressor, which may drive unwanted collective effects such as CSR and longitudinal wakefields in the undulators [72]. To solve the problem, an X-band accelerating structure (H60VG3) and an X-band klystron (XL-4) were introduced. The measured attenuation of the acceleration structure was about 4.8 dB, and the required RF power was calculated to be 30 MW for the X-band accelerating structure. To obtain 30 MW RF power from the klystron output, a 1 kW driver source was selected after considering the cable attenuation from the driver amplifier to the klystron.

At the beginning of the PAL-XFEL project, a travelling-wave tube amplifier (TWTA) was considered as a driver amplifier for the X-band klystron, because it can generate more than 1 kW RF powers with high efficiency. However, the TWTA could not meet the requirement of the RF amplitude and phase stabilities of PAL-XFEL. The stability requirements for the amplitude and phase are 0.06% and 0.1°, respectively. Eventually, a solid-state amplifier (SSA) was developed on the base of GaN high-electron-mobility transistors (HEMTs) with a power-combining method [73]. The SSA has been used as an alternative to vacuum-tube-based amplifiers recently, owing to the low supply voltage, low unit cost, and longer lifetime than the TWTA. These features are also attractive from the viewpoint of accelerator maintenance. The newly developed SSA has a twenty-way power divider and combiner, based on hybrid rectangular and radial waveguide-type, spatial power-combining method [74]. The measured amplitude and phase stabilities were 0.04% and 0.07°, respectively. By using the same setup, we also measured the amplitude and phase stabilities of a commercial TWTA (174X, Applied Systems Engineering) which generates RF pulses of 1 kW at 11.424 GHz. The measured amplitude and phase stabilities of the TWTA were 0.07% and 0.15°, respectively [75].

Table 7 Major specifications of the S-band deflecting cavity

Parameters	Specifications
Operation frequency	2856 MHz
Operation mode	$2\pi/3$
Length	2.7 m
Q	> 1190
Attenuation	2.7 dB
Filling time	418 ns
Deflecting voltage	20 MV

4 Undulator

4.1 Undulator

The European XFEL undulator design is well-proven for standardization and optimization for the mass production of 91 undulators for European XFEL [76–78]. The European XFEL undulator design features a unique pole height tuning mechanism that enables moving a pole height using locking screws. For the PAL-XFEL undulator, the European XFEL undulator design was adopted and modified. The pole height tuning scheme is fully utilized to tune all undulators, and it was essential in speeding up the undulator preparation. Moreover, the magnetic gap and period were changed with new magnetic geometry reflecting PAL-XFEL requirements. All tolerances were recalculated by changing the magnetic geometry and found to be more stringent than the European-XFEL undulator case. In addition, precision tiltmeters were attached to the girders to monitor the tilting and tapering of the undulator. Figure 7 shows the undulator for PAL-XFEL.

The local-K pole tuning procedure was developed and applied to all fabricated undulators. For the field corrections, three nearest-neighbor poles were included in the correction signatures, and a single iteration of pole height tuning could reduce the local-K fluctuations by one order of magnitude. After the local-K tuning at the given undulator gap, the maximum phase error was about 2° which was acceptable for PAL-XFEL. Even if the undulator is tuned perfectly at the tuning gap, the phase error can be increased when the undulator gap is changed. As the undulator gap deviated from the tuning gap, the magnet girder deformed into a parabolic shape, and the phase jit-

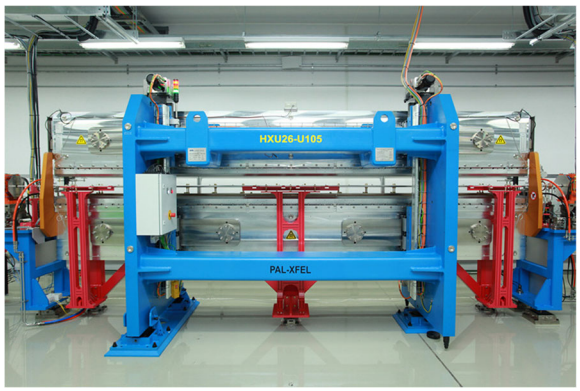

Fig. 7 The undulator for PAL-XFEL

ter showed a typical S-structure which is the signature of the parabolic bending. For all operating gaps ranging from 8.3 to 12.5 mm for hard X-ray undulators, the phase jitter met the specification of 7° for PAL-XFEL. All other undulator properties, like entrance and exit kicks, were also calculated from the magnetic measurements. Table 8 shows the major specification of the PAL-XFEL undulator.

The deflection parameter K increases when the electron beam moves away from the midplane. In this case, the undulator gap should be increased to compensate for the increased K coming from the vertical offset. To minimize this error, the optical measurement of undulator spontaneous radiation was introduced to find the undulator midplane offset, and this feature was used to align the undulator midplane in SACLA [79]. The undulator control system of PAL-XFEL was modified to enable the movement of the undulator midplane within ± 300 μm by translating the magnet girders in the same direction. This feature is essential to estimate the undulator midplane in the optical measurement of spontaneous radiation. In addition, all safety features were implemented to avoid mechanical interference with vacuum chambers and mechanical hard stops [80].

4.2 Cavity beam position monitor

For the saturation of the FEL radiation, the overlap between the electron beam and FEL radiation in the undulators is critically important to make the micro-bunching inside the electron beam. Thus, the electron beam orbit should be maintained straight within the electron beam size to keep the interaction between the electron and photon beam. In the case of PAL-XFEL, the FEL power reduction is 20% of the perfectly aligned case when the alignment error of the beam trajectory is 12 μm, so that the alignment error should be less than 5 μm for the stable operation [81]. To maintain the electron beam trajectory within a few μm, cavity-type beam position monitors (BPMs) with sub-μm resolution are required in the Section 4. Table 9 shows the requirements of the cavity BPM for PAL-XFEL.

The PAL-XFEL cavity BPM consists of two cylindrical cavities. One is the reference cavity and the other is the XY cavity. The reference cavity measures the beam charge and provides a reference phase for the XY cavity using the monopole mode. The XY cavity measures the beam position using the dipole mode. The structure of the reference cavity is designed as simple as possible for easy fabrication because the RF parameter of the X-band structure is highly sensitive to fabrication error. According to the error tolerance study using CST MWS, a machining error of ± 10 μm made a frequency change of ± 5 MHz in the resonant mode of each cavity. Thus, the machining tolerance was set as 10 μm and a tuning structure was introduced for each cavity to compensate for mechanical errors. The antenna of the SMA feed-through is connected to the reference cavity directly using a power coupling hole.

In the case of the XY cavity, the monopole mode can be excited in addition to the dipole mode and the mode selection is an issue for the cavity BPM design. To solve the problem, a selective coupler was proposed for the LCLS cavity BPM pick-up design, and the suppression of the monopole mode was obtained by using the selective coupler structure between the cavity and the output waveguide [82]. In the PAL-XFEL cavity BPM, an additional waveguide was introduced as a selective coupler. Because of the waveguide geometry for the magnetic field

Table 8 Major specifications of the PAL-XFEL undulator

Parameters	Hard X-ray	Soft X-ray
Beam energy	10.0 GeV	3.15 GeV
Minimum gap	8.30 mm	9.00 mm
Period	26.0 mm	35.0 mm
Length	5 m	5 m
B_{eff}	0.812 T	1.016 T
K	1.973	3.321
Phase Jitter	$\leq$ 7.0°	$\leq$ 7.0°

Table 9 Requirements for the cavity BPM of PAL-XFEL

Parameters	Reference Cavity	Dipole Cavity
Frequency	11.424 GHz	11.424 GHz
Mode	TM010	TM110
Loaded Q	2000 $\sim$ 3000	2000 $\sim$ 3000
R/Q	12 Ω	2 Ω/mm
Induced Voltage	20 mV/pC	5 mV/pC·mm
X/Y Cross Talk	-	$<$ −20 dB

coupling, only the dipole mode propagates into the output waveguide which is connected to the SMA feed-through.

In the case of X-band frequency, commercial SMA feed-throughs were not available for high vacuum, and a coaxial type SMA feed-through had to be designed and fabricated. For the fabrication of the SMA feed-through, a female SMA connector, ceramic insulator for the vacuum and RF power sealing, and antenna for the collection of the electromagnetic signal should be brazed to make an inner part. In the prototype fabrication, we noticed that the optimization of the brazing process and amount of the brazing alloy were critically important for the feed-through performance in the X-band region, and sheet-type brazing alloys were used to minimize the brazing alloy overflow [83].

In PAL-XFEL, cavity BPMs were installed for all undulator units together with quadrupole magnets as shown in Fig. 8. Cavity BPM pickups were combined with the modified LCLS cavity BPM electronics, which showed good stability of 71 μm for 24 h and a resolution better than 1 μm [84]. In the electronics, the cavity BPM signals are downmixed from 11.424 GHz to 25 $\sim$ 60 MHz using a four-channel heterodyne receiver, and the signals are digitized to 16 bits at a 119 MHz sampling rate in four-channel μTCA digitizers designed by SIS. Waveforms are transmitted over the backplane to a μTCA processor which reduces raw waveforms to beam position and charge. An EPICS IOC communicated with the receiver via UDP messages, and the receiver responds to commands and requests from the IOC. The IOC polls the receiver periodically for current register values and monitoring signals and provides this data via EPICS Process Variables (PVs) [85].

5 Summary

From the electron gun to the undulator, lots of devices were installed inside the PAL-XFEL tunnel to produce FEL radiation with an ultra-small jitter. They had been designed, fabricated, and tested with newly developed technologies in PAL, based on help from the accelerator community around the world. The injector layout and parameters were optimized to obtain the minimum emittance of the electron beam and ITF was constructed to demonstrate the performance of the PAL-XFEL injector. The multi-pole fields in the photocathode RF gun were removed using the four-holed gun cavity. The laser heater was optimized to remove CSR-induced MBI by controlling the uncorrelated energy spread of the electron beam. The RF timing system, SSA, LLRF, and modulators were significantly upgraded to provide stable RF power for the electron beam acceleration. The SLED was newly designed for the 80 MW klystron and matched with the accelerating column which has J-type, quasi-symmetry, or racetrack-shaped couplers. The design of the European XFEL undulator was adopted for the PAL-XFEL undulator. However, upgrades were made in many parts and the offset change of the magnet girders was applied for the optical tunning of the undulator midplane. The cavity BPM was developed for the alignment of the electron beam trajectory in the Section 4 and the sub-μm resolution was achieved. All of these technical achievements have been a strong foundation for the successful construction of PAL-XFEL.

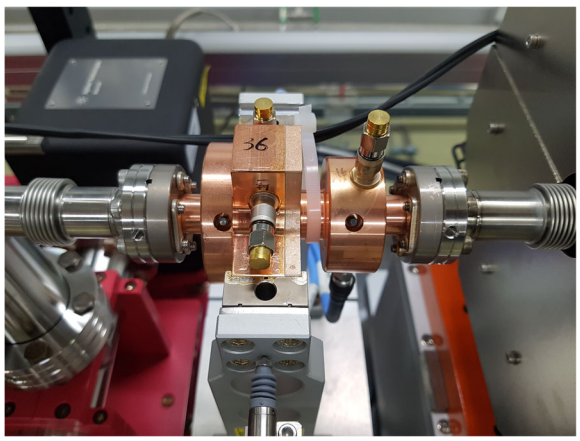

Fig. 8 The cavity BPM in the PAL-XFEL undulator section

Acknowledgements
The authors acknowledge Prof.W. Namkung for giving them the valuable opportunity to write this review article. The authors appreciate all members of PAL-XFEL for their great contribution to the PAL-XFEL construction.

Authors' contributions
The authors read and approved the final manuscript.

Authors' information
Changbum Kim is a Senior Researcher at Pohang Accelerator Laboratory and Head of the Accelerator Division in PAL-XFEL.

Funding
Not applicable.

Availability of data and materials
Not applicable.

Declarations

Ethics approval and consent to participate
Not applicable.

Consent for publication
Not applicable.

Competing interests
The authors declare that they have no competing interests.

Author details
[1] Pohang Accelerator Laboratory, POSTECH, Pohang 37673, Korea. [2] Korea Atomic Energy Research Institute, Daejeon 34057, Korea.

Received: 14 March 2022 Accepted: 25 April 2022
Published online: 01 June 2022

References

1. P. Emma, et al., First lasing and operation of an angstrom-wavelength free electron laser. Nat. Photon. **4**, 641 (2010)
2. T. Ishikawa, et al., A compact X-ray free-electron laser emitting in the sub-angstrom region. Nat. Photon. **6**, 540 (2012)
3. T. Ishikawa, SACLA: The SPring-8 Angstrom Compact Free Electron Laser. AAPPS Bull. **26**(1), 5 (2016)
4. I. S. Ko, Status of PAL-XFEL construction. AAPPS Bull. **26**(1), 25 (2016)
5. H.-S. Kang, et al., Hard X-ray free-electron laser with femtosecondscale timing jitter. Nat. Photon. **11**, 708 (2017)
6. W. Decking, et al., A MHz-repetition-rate hard X-ray free-electron laser driven by a superconducting linear accelerator. Nat. Photon. **14**, 391 (2020)
7. E. Prat, et al., A compact and cost-efective hard X-ray free-electron laser driven by a high-brightness and low-energy electron beam. Nat. Photon. **14**, 748 (2020)
8. T. O. Raubenheimer, in *Proc. FEL2015*. LCLS-II: status of the CW X-ray FEL upgrade to the SLAC LCLS facility (JACoW, Daejeon, 2015), p. 618
9. D. Wang, et al., in *Proc. ICAP2018*. SHINE: Shanghai high rep-rate XFEL and extreme light facility (JACoW, Key West, 2018). SUPAG07
10. S. H. Nam, PLS-II starts user service. AAPPS Bull. **22**(2), 16 (2012)
11. S. Shin, Commissioning of the PLS-II. J. Instrum. **8**, P01019 (2013)
12. S. Shin, New era of synchrotron radiation: fourth generation storage ring. AAPPS Bull. **31**(1), 21 (2021)
13. Pohang X-ray Free Electron Laser Facility Conceptual Design Report (PAL, Pohang, 2011)
14. H.S. Kang, et al., *PAL-XFEL Technical Design Report*. (PAL, Pohang, 2014)
15. S. Reiche, Compensation of FEL gain reduction by emittance effects in a strong focusing lattice. Nucl. Instrum. Meth. A. **445**, 90 (2000)
16. S. J. Park, et al., in *Proc. IPAC2013*. Construction of Injector Test Facility (ITF) for the PAL XFEL (JACoW, Shanghai, 2013), p. 2220
17. B. E. Carlsten, New photoelectric injector design for the Los Alamos National Laboratory XUV FEL accelerator. Nucl. Instrum. Meth. A. **285**, 313 (1989)
18. J.-H. Han, et al., in *Proc. IPAC2012*. Injector design for PAL-XFEL project (JACoW, New Orleans, 2012), p. 1732
19. R. Akre, et al., Commissioning the Linac Coherent Light Source injector. Phys. Rev. ST Accel. Beams. **11**, 030703-1 (2008)
20. J.-H. Han, in *Proc. IPAC2016*. Beam commissioning of PAL-XFEL (JACoW, Busan, 2016), p. 6
21. E. Prat, et al., General and efficient dispersion-based measurement of beam slice parameters. Phys. Rev. ST Accel. Beams. **17**, 032801 (2014)
22. F. Brinker, in *Proc. IPAC2016*. Commissioning of the European XFEL injector (JACoW, Busan, 2016), p. 1044
23. J. Hong, et al., in *Proc. FEL2014*. Beam measurement of photocathode RF-gun for PAL-XFEL (JACoW, Basel, 2014), p. 699
24. K. J. Kim, RF and space-charge effects in laser-driven RF electron guns. Nucl. Instrum. Meth. A. **275**, 201 (1989)
25. D. H. Dowell, et al., *The development of the Linac Coherent Light Source RF gun. SLAC-PUB-13401*. (SLAC, Menlo Park, 2008)
26. K. Batchelor, et al., in *Proc. EPAC90*. Operational status of the Brookhaven National Laboratory Accelerator Test Facility (JACoW, Nice, 1990), p. 541
27. D. T. Palmer, et al., in *Proc. PAC95*. Microwave measurements of the BNL/SLAC/UCLA 1.6 cell photocathode RF gun (JACoW, Dallas, 1995), p. 982
28. J. B. Rosenzweig, et al., in *Proc. PAC99*. The effects of RF asymmetries on photoinjector beam quality (JACoW, New York, 1999), p. 2042
29. C. Limborg, et al., *RF design of the LCLS gun. SLAC-TN-10-094*. (SLAC, Menlo Park, 2005)
30. L. Xiao, et al., in *Proc. PAC2005*. Dual feed RF gun design for the LCLS (JACoW, Knoxville, 2005), p. 3432
31. J. H. Park, et al., High power beam test and measurement of emittance evolution of a 1.6-cell photocathode RF gun at Pohang Accelerator Laboratory. Jpn. J. Appl. Phys. **46**, 1751 (2007)
32. S. I. Moon, et al., Reduction of multipole fields in photocathode RF gun. Jpn. J. Appl. Phys. **49**, 086401 (2010)
33. J. Hong, et al., High-power beam test of the photocathode RF gun at the Pohang Accelerator Laboratory. J. Korean Phys. Soc. **58**, 198 (2011)
34. Y. W. Parc, et al., Accurate method for estimating of the charge in the bunching part of an electron beam by using an electro-optic crystal. J. Korean Phys. Soc. **54**, 1481 (2009)
35. M. S. Chae, et al., Emittance growth due to multipole transverse magnetic modes in an RF gun. Phys. Rev. ST Accel. Beams. **14**, 104203 (2011)
36. J. Lee, et al., Parameter optimization of PAL-XFEL injector. J. Korean Phys. Soc. **72**, 1158 (2018)
37. Z. Huang, et al., Suppression of microbunching instability in the linac coherent light source. Phys. Rev. ST. Accel. Beams. **5**, 074401 (2002)
38. S. Heifets, et al., Coherent synchrotron radiation instability in a bunch compressor. Phys. Rev. ST. Accel. Beams. **5**, 064401 (2002)
39. M. Borland, et al., Start-to-end simulation of self-amplified spontaneous emission free electron lasers from the gun through the undulator. Nucl. Instrum. Meth. A. **483**, 268 (2002)
40. T. Limberg, et al., An analysis of longitudinal phase space fragmentation at the TESLA test facility. Nucl. Instrum. Meth. A. **475**, 353 (2001)
41. E. L. Saldin, et al., Longitudinal space charge-driven microbunching instability in the TESLA test facility linac. Nucl. Instrum. Meth. A. **528**, 355 (2004)
42. Z. Huang, et al., Suppression of microbunching instability in the linac coherent light source. Phys. Rev. ST. Accel. Beams. **7**, 074401 (2004)
43. Z. Huang, et al., Measurements of the linac coherent light source laser heater and its impact on the x-ray free-electron laser performance. Phys. Rev. ST. Accel. Beams. **13**, 020703 (2010)
44. S. Spampinati, et al., Laser heater commissioning at an externally seeded free-electron laser. Phys. Rev. ST. Accel. Beams. **17**, 120705 (2014)
45. M. Hamberg, et al., in *Proc. FEL2015*. Construction of the EU-XFEL laser heater (JACoW, Daejeon, 2015), p. 452
46. M. Pedrozzi, et al., in *Proc. FEL2014*. The laser heater system of SwissFEL (JACoW, Basel, 2014), p. 871
47. J. Lee, et al., PAL-XFEL laser heater commissioning. Nucl. Instrum. Meth. A. **843**, 39 (2019)
48. K. Jung, et al., Remote laser-microwave synchronization over kilometer-scale fiber link with few-femtosecond drift. J. Lightw. Tech. **32**, 3742 (2014)
49. C.-K. Min, et al., in *Proc. IPAC2016*. RF timing distribution and laser synchronization commissioning of PAL-XFEL (JACoW, Busan, 2016), p. 4234
50. M. Borland, in *Proc. ICAP2000*. Elegant: a flexible SDDS-compliant code for accelerator simulation (INSPIRE, Darmstadt, 2000). LS-287
51. H. Yang, et al., in *Proc. IPAC2014*. Linac lattice optimization for PAL-XFEL hard X-ray FEL line (JACoW, Dresden, 2014), p. 2900
52. S. H. Kim, et al., in *Proc. FEL2015*. PAL XFEL pulse modulator system test results using a high precision CCPS (JACoW, Daejeon, 2015), p. 89
53. J. Hu, et al., in *Proc. IPAC2016*. Development of an X-band linearizer system for PAL-XFEL (JACoW, Busan, 2016), p. 554
54. H.-S. Lee, et al., in *Proc. IPAC2016*. PAL-XFEL linac RF system (JACoW, Busan, 2016), p. 3192
55. P. B. Wilson, *A method for doubling SLAC's energy. SLAC-TN-73-15*. (SLAC, Menlo Park, 1973)
56. Z. D. Farkas, et al., *SLED: A method of doubling SLAC's energy. SLAC-PUB-1453*. (SLAC, Menlo Park, 1974)
57. Z. D. Farkas, et al., Recent progress on SLED-The SLAC Energy Doubler. IEEE Trans. Nucl. Sci. **NS-22**, 1299 (1975)
58. CST Microwave Studio 2014. https://www.cst.com. Accessed 11 May 2022
59. A. Fiebig, et al., *Design considerations: construction and performance of a SLED-type radiofrequency pulse compressor using very high Q cylindrical cavities. CERN/PS 87-45*. (CERN, Geneva, 1987)
60. H. Matsumoto, et al., High power test of a SLED system with dual side-wall coupling irises for linear colliders. Nucl. Instrum. Meth. A. **330**, 1 (1993)
61. Y. Joo, et al., Development of new S-band SLED for PAL-XFEL linac. Nucl. Instrum. Meth. A. **843**, 50 (2019)
62. R. B. Neal, *The Stanford Two-Mile Accelerator*. (W. A. Benjamin Inc., 1968)
63. Z. Li, et al., in *Proc. PAC2005*. Coupler design for the LCLS injector S-band structures (IEEE, Knoxville, 2005), p. 2176
64. C. Suzuki, et al., in *Proc. PAC97*. Input coupler design for C-band accelerating structure (JACoW, Vancouver, 1997), p. 536
65. S. Miura, et al., in *Proc. FEL2012*. Developing S-band accelerating structures (JACoW, Nara, 2012), p. 153
66. J. Haimson, et al., A racetrack geometry to avoid undesirable azimuthal variations of the electric field gradient in high power coupling cavities for TW structures. AIP Conf. Proc. **398**, 898 (1997)
67. H. Heo, et al., Development of an S-band accelerating structure with quasi-symmetric single-feed racetrack couplers. J. Korean Phys. Soc. **66**, 905 (2015)

68. O. H. Altenmueller, et al., Investigations of Traveling-Wave Separators for the Stanford Two-Mile Linear Accelerator. Rev. Sci. Inst. **35**, 438 (1964)
69. J. W. Wang, et al., *X-band traveling wave RF deflector structures. SLAC-PUB-5321*. (SLAC, Menlo Park, 1990)
70. N. M. Kroll, et al., *Applications of time domain simulation to coupler design for periodic structures. SLAC-PUB-8614*. (SLAC, Menlo Park, 2000)
71. H. Heo, et al., S-band traveling-wave deflecting structures for the PAL-XFEL. J. Korean Phys. Soc. **73**, 1099 (2018)
72. P. Emma, *X-band RF harmonic compensation for linear bunch compression in the LCLS. SLAC-TN-05-004*. (SLAC, Menlo Park, 2001)
73. S. H. Lee, et al., in *Proc. APMC2016*. X-band 1kW SSPA using 20-way hybrid radial combiner for accelerator (IEEE, New Delhi, 2016). 16901684
74. K. Song, et al., Ku-band 200-W pulsed power amplifier based on waveguide spatially power-combining technique for industrial applications. IEEE Trans. Ind. Electron. **61**, 4274 (2014)
75. H. Heo, et al., X-band amplifier for the PAL-XFEL. J. Korean Phys. Soc. **76**, 573 (2020)
76. J. Pflueger, et al., Field fine tuning by pole height adjustment for the undulator of the TTF-FEL. Nucl. Instrum. Meth. A. **429**, 386 (1999)
77. U. Englisch, et al., in *Proc. FEL2012*. Tuning and testing of the prototype undulator for the European XFEL (JACoW, Nara, 2012), p. 579
78. J. Pflueger, et al., in *Proc. FEL2013*. Shimming strategy for the phase shifters used in the European XFEL (JACoW, New York, 2013), p. 313
79. T. Tanaka, et al., Undulator commissioning by characterization of radiation in X-ray free electron lasers. Phys. Rev. ST Accel. Beams. **15**, 110701 (2012)
80. D.-E. Kim, et al., Development of PAL-XFEL undulator system. J. Korean Phys. Soc. **71**, 744 (2017)
81. Y. W. Parc, et al., Automation of beam based alignment for the PAL-XFEL undulator line. Nucl. Instr. and Meth. A. **782**, 120 (2015)
82. Z. Li, et al., in *Proc. PAC2003*. Cavity BPM with dipole-mode-selective coupler (JACoW, Portland, 2003). ROAB004
83. S. Lee, et al., PAL-XFEL cavity beam position monitor pick-up design and beam test. Nucl. Instrum. Meth. A. **827**, 107 (2016)
84. S. Smith, et al., in *Proc. PAC09*. Commissioning and performance of LCLS cavity BPMs (JACoW, Vancouver, 2009), p. 754
85. A. Young, et al., in *Proc. IBIC2013*. Performance measurements of the new X-band cavity BPM receiver (JACoW, Oxford, 2013), p. 735

Publisher's Note